THE UNIVERSITY *of* EDINBURGH

Edinburgh Research Explorer

In Vivo Tumor Visualization through MRI Off-On Switching of NaGdF4–CaCO3 Nanoconjugates

OPEN ACCESS

In Vivo Tumor Visualization through MRI Off-On Switching of NaGdF$_4$–CaCO$_3$ Nanoconjugates

Zhigao Yi, Zichao Luo, Nicole D Barth, Xianfu Meng, Hong Liu, Wenbo Bu, Angelo All, Marc Vendrell, and Xiaogang Liu*

Zhigao Yi, Zichao Luo, Prof. X. Liu
Department of Chemistry, National University of Singapore, Singapore 117543, Singapore
E-mail: chmlx@nus.edu.sg

Nicole D Barth, Dr. M. Vendrell
Centre for Inflammation Research, Queen's Medical Research Institute, The University of Edinburgh, EH16 4TJ Edinburgh, United Kingdom

Xianfu Meng, Prof. W. Bu
Shanghai Key Laboratory of Green Chemistry and Chemical Processes, College of Chemistry and Molecular Engineering, East China Normal University, Shanghai 200062, China

Prof. H. Liu
State Key Laboratory of Crystal Materials, Shandong University, Jinan 250100, China

Prof. H. Liu
Institute for Advanced Interdisciplinary Research (IAIR), University of Jinan, Jinan 250022, China

Prof. A. All
Department of Biomedical Engineering, School of Medicine, Johns Hopkins University, Baltimore, MD 21205, USA

Prof. X. Liu
Singapore Institute of Neurotechnology (SINAPSE), National University of Singapore, Singapore 117456, Singapore

Abstract: The development of high-performance contrast agents in magnetic resonance imaging (MRI) has recently received considerable attention, as they hold great promise and potential as a powerful tool for cancer diagnosis. Despite substantial achievements, it remains challenging to develop nanostructure-based biocompatible platforms that can generate on-demand MRI signals with high signal-to-noise ratios and good tumor specificity. In this article, we report the design and synthesis of a new class of nanoparticle-based contrast agents comprising self-assembled NaGdF$_4$ and CaCO$_3$ nanoconjugates. In our design, the spatial confinement of the T$_1$ source (Gd^{3+} ions) leads to an "OFF" MRI signal due to insufficient interaction between the protons and the crystal lattices. However, when immersed in a mildly acidic tumor microenvironment, the embedded CaCO$_3$ nanoparticles generate CO$_2$ bubbles and subsequently disconnect the nanoconjugate, thus resulting in an "ON" MRI signal. The *in vivo* performance of this nanoconjugates shows more than 60-fold contrast enhancement in tumor visualization relative to commercially used contrast agent

Magnevist. Our work presents a significant advance in the construction of smart MRI nanoprobes ideally suited for deep-tissue imaging and target-specific cancer diagnosis.

Magnetic resonance imaging (MRI) is a powerful technique for noninvasive disease diagnosis and therapeutic monitoring. MRI can provide invaluable details of anatomical structures, which stem from the subtle interactions between water protons and biomolecules in surrounding tissues.[1-4] However, MRI images often suffer from poor spatial resolution due to limited differences between dynamic microenvironments in healthy and diseased tissues.[5,6] Therefore, exogenous agents are generally required to enhance the contrast and enable the differentiation of anatomical lesions from healthy tissues.[7-9] MRI contrast agents are classically divided into two categories based on the imaging modalities, where longitudinal and transversal relaxation time of protons is shortened, resulting in positive or negative signal enhancements in T_1- or T_2-weighted MRI, respectively, when an appropriate pulse sequence is applied.[10,11] The well-established positive contrast agents generally contain inorganic nanoparticles or organic complexes fused with metal ions, such as gadolinium (Gd^{3+}),[12,13] iron,[14-16] or manganese.[17,18] The past decade has witnessed the widespread use of Gd^{3+}-based chelation complexes (e.g., Magnevist) as clinical imaging agents, primarily due to their excellent contrast enhancement and negligible immunogenicity. Gd^{3+} essentially holds an electronic relaxation rate of 6 orders of magnitude slower than other lanthanides because of its seven unpaired electrons occupying at the ground state ($^8S_{7/2}$),[19] which makes Gd^{3+} suitable as an excellent T_1-source. However, Gd^{3+}-based commercial agents have two severe limitations: short circulating time and lack of specificity *in vivo*. These drawbacks inevitably lead to low signal-to-noise ratios (SNR), an increased risk of Gd^{3+} retention and the need for high dose regimes.

To address these issues, considerable efforts have been devoted to the development of Gd^{3+}-based inorganic nanoparticles featuring different morphologies, sizes, and surface functional groups.[20-22] Given the extensive exposure of Gd^{3+} ions, ultrasmall Gd^{3+}-based nanoparticles are characterized with ideal longitudinal relaxivity.[23] However, they are restricted by their short-time

circulation in the blood due to fast renal clearance, which hinders their utility in real-time tracking and visualization of lesions. Recently, $CaCO_3$ and $CaPO_4$ nanoparticles have been used as host materials for pH sensing and controlled release of manganese ions and drugs at tumor sites.[24,25] In addition, nanostructures assembled by magnetic nanoparticles have emerged as negative contrast agents for MRI.[26-28] We reasoned that self-assembled $NaGdF_4$-$CaCO_3$ nanoconjugates that could be encapsulated by cell membrane cloaking would provide an all-in-one MRI nanoplatform with high tumor selectivity and good biocompatibility (Figure 1a).

In our design, we hypothesized that the MRI imaging signals of $NaGdF_4$-$CaCO_3$ nanoconjugates would be initially blocked because of the structural separation of $NaGdF_4$ nanoparticles from water protons, and subsequently recovered under acidic conditions due to the CO_2-triggered release of $NaGdF_4$ nanoparticles. In the presence of activated T_1 source, the protons in resonance with the radiofrequency can rapidly relax to their initial spin state with a recovery of the net magnetization aligned to the direction of the magnetic field (M_Z) (Figure 1b). Therefore, $NaGdF_4$ nanoparticles released from the nanoconjugates facilitate the energy transfer from protons to Gd^{3+} ions through spin-lattice interaction, leading to a shortened longitudinal relaxation time, faster recovery of M_Z and ultimately brighter images.

To verify our hypothesis, ultrasmall $NaGdF_4$ nanoparticles with an average size of 3.6 nm were first synthesized *via* a co-precipitation method (Figure S1).[29] Then, we prepared $CaCO_3$ nanoparticles (~18 nm) that were highly responsive to a mildly acidic environment by a gas diffusion reaction (Figure S2).[24] The mixture of $NaGdF_4$ nanoparticles and PLGA in dichloromethane was added into a flask containing Pluronic F-127 and $CaCO_3$ nanoparticles in deionized water. The hydrophobic interaction between nanoparticles and polymers resulted in the formation of milky white emulsion after 5 minutes of sonication. Uniform bare self-assembled nanoparticles (BSNPs) were generated by adding branched polyethylenimine (PEI), followed by overnight agitation at room temperature to evaporate the organic solvent (Figure 2a). Statistical analysis of the transmission electron microscopy (TEM) images showed a mean particle diameter of

142 nm with a narrow size distribution (Figure S3a). X-ray powder diffraction and energy dispersive X-ray spectroscopy indicated the presence of $NaGdF_4$ and $CaCO_3$ nanoparticles inside BSNPs (Figures S4 and S5). An essential advantage of using branched PEI is to facilitate the formation of homogeneous BSNPs by suppressing the recombination of emulsion droplets (Figure S6). The positively charged PEI layer also facilitated the cloaking of negatively-charged cell membranes onto the surface of BSNPs due to their electrostatic interaction and the formation of amide bonds between branched PEI and phospholipids or proteins (Figure S7).[30] TEM imaging analysis showed the average diameter of cell membrane coated-BSNPs (MSNPs) was 191 nm (Figure 2b,c and Figure S3b).

To further validate the successful coating of $NaGdF_4$–$CaCO_3$ nanoconjugates with membranes derived from HeLa cells, we labeled BSNPs and HeLa cell membranes with green-fluorescent fluorescein isothiocyanate (FITC) and red-fluorescent anti-*p*-Cadherin antibody, respectively. This protocol allowed us to observe overlay images of green and red emissive spots from membrane-coated nanostructures under luminescence microscopy (Figure 2d). In contrast, BSNPs showed only green emission spots (Figure 2e). The successful membrane coating was also confirmed by dynamic light scattering and zeta potential measurements. As shown in Figure 2f, the hydrodynamic size of BSNPs increased from ~178 to ~215 nm after coating. In addition, the zeta potential of MSNPs turned negative, which contrasts with the positive value of BSNPs (Figure 2g). Moreover, the potential observed for MSNPs (-24 mV) was very similar to pure HeLa cell membranes, indicating that the HeLa cell membranes fully covered the surface of MSNPs.[31-33] To verify the biomimetic functionality of the decorated MSNPs, we also measured the concentration of *p*-Cadherin in BSNPs and MSNPs by ELISA (enzyme-linked immunosorbent assay).[34] The observed high levels of *p*-Cadherin in MSNPs but not in BSNPs indicated a similar surface configuration for MSNPs when compared to HeLa cell membranes (Figure 2h).

We further investigated the structural stability of MSNPs. To our delight, we detected no apparent changes in the morphology of MSNPs that were stored under phosphate buffer solution

(pH 7.4) for up to two weeks (Figure S8). The dynamic light scattering measurement also showed a negligible increase in hydrodynamic size (Figure S9), which confirmed the high stability of MSNPs. In contrast, BSNPs exhibited a marked change in both the hydrodynamic size and the shape under identical experimental conditions. Taken together, the improved structural stability of MSNPs over BSNPs can be attributed to the cloaking of nanostructures with cell membranes.

We next tested the suitability of $CaCO_3$ nanoparticles embedded in MSNPs as pH sensors in response to the acidic environment found in most tumors. As illustrated in Figure 3a, encapsulated $CaCO_3$ nanocrystals can generate CO_2 bubbles *in situ* under mildly acidic conditions, which leads to the rapid disintegration of the self-assembled nanoconjugates. In our *in vitro* experiments with different pH buffer solutions, we observed that the surface membrane started disassembling at pH 6 (Figure 3b), and the nanoconjugates were fully disintegrated at pH 5. A similar pH response was also observed for BSNPs (Figure S10).

We also performed negative control experiments by synthesizing self-assembled nanostructures without incorporating $CaCO_3$ nanoparticles to demonstrate that multilayered structures remained intact in neutral and mildly acidic conditions (Figures S11 and S12). Notably, in contrast to MSNPs, the morphology of BSNPs containing $CaCO_3$ nanoparticles did not remain uniform, and their structure appeared to be unstable (Figure S13). This observation highlights that the ratio of $NaGdF_4$ to $CaCO_3$ is a key factor to achieve an optimal balance between structural stability at neutral pH and *in situ* activation in acidic microenvironments.

To verify the feasibility of using MSNPs as smart contrast agents with high sensitivity to the acidic microenvironment in tumors, we monitored their longitudinal relaxivity changes *in vitro* under different conditions. The longitudinal relaxivity (r_1) of MSNPs was relatively low (0.79 mM^{-1}s^{-1}) at neutral pH (Figure 3c), whereas its r_1 value sharply increased in acid media, with an over 10-fold increase from pH 7.4 to 5.0. The corresponding T_1-weighted phantom images (Figure 3d) also showed a significant improvement of the contrast signals when the solutions became acidic. At the beginning, water protons only directly interact with limited $NaGdF_4$ nanoparticles which are located

at the outer layer of the nanoconjugates. When water protons react with $CaCO_3$ from the outside to inside, $NaGdF_4$ nanoparticles at the same layers could be simultaneously released through a layer-by-layer exfoliation. The large amount of the released ultra-small $NaGdF_4$ nanoparticles results in a significant MRI signal enhancement, while the initial form of nanoconjugates with inefficient interaction with protons gives a limited signal enhancement. In addition, we performed the same experiments in BSNPs and observed good relaxivity and contrast enhancement *in vitro* (Figure S14). This observation highlights that the HeLa cell membrane layer has no significant effect on the sensitivity of BSNPs to acid microenvironments or the release of $NaGdF_4$ nanoparticles.

We measured the cytotoxicity of BSNPs and MSNPs in different cell lines (RAW 264.7, NIH 3T3 and HeLa cells) using the 3-(4,5-dimethylthiazol-2-yl)-2,5-diphenyltetrazolium bromide (MTT) assay. In all cases, cell viabilities were over 80 %, even when using concentrations of BSNPs and MSNPs at 200 µg/mL (Figure S15), which indicates good biocompatibility. Next, we examined the specific targeting properties of MNSPs to homogenous HeLa cells by flow cytometry experiments. MSNPs exhibited preferential uptake in HeLa cells (Figure 3e,h), while both BSNPs and MSNPs presented relatively low cellular uptake in HepG2 cells (Figure 3f,i), highlighting the homogenous tumor-targeting capabilities of MSNPs. To better understand the active uptake of MSNPs in HeLa cells, we compared their internalization in untreated cells and in cells pre-treated with cytochalasin D, a potent inhibitor of actin polymerization that blocks active transport. We observed that the uptake of MSNPs by HeLa cells was blocked to the levels of BSNPs (Figure 3g,j). This result suggests that cell surface recognition is essential to facilitate the active internalization of MSNPs in HeLa cells.

To validate the MRI contrast enhancement effect at the cellular level, we also acquired T_1-weighted MRI phantom images of HeLa cells microgel solutions containing PBS buffer, BSNPs or MSNPs. As shown in Figure 3k, we demonstrated that remarkably brighter phantom images with significantly enhanced positive contrast were obtained from Hela cells that had been incubated with MSNPs but not with BSNPs or in the PBS control group, validating the active internalization of

6

MSNPs and the release of $NaGdF_4$ nanoparticles in HeLa cells. Finally, we also assessed the half-life of both BSNPs and MSNPs by tracking the content of Gd^{3+} ions in venous blood samples *via* inductive coupled plasma-optical emission spectroscopy. The results indicate that the HeLa cell membrane coating endows a prolonged *in vivo* circulation time (Figure S16), which enhances the targeting properties of MSNPs by the enhanced permeability and retention effect.

The promising *in vitro* performance of MSNPs prompted us to investigate their contrast capabilities *in vivo*. As a proof-of-concept, we prepared subcutaneous tumor-bearing mice with HeLa cells transplants to study the behavior of MSNPs in animal models. T_1-weighted MR images were acquired *in vivo* before and after intravenous injection of MSNPs. The tumor site appeared as dark before the injection of MSNPs and started lighting up approximately 30 min post-injection (Figure 4a,c and Figure S17). The contrast enhancement at the tumor site reached a tumor-to-background (T/B) ratio of ~48 at 195 min post-injection when the entire tumor was lighted up. Next, Magnevist, a representative of clinical contrast agents, was chosen as a control contrast agent due to its widespread use for clinical applications and its facile accessibility. We injected Magnevist intravenously and monitored its accumulation over time. In contrast to MSNPs, the entire body, including tumor site, muscles, and especially the bladder, were lighted up after 30 min post-injection (Figure 4b and Figure S17). The bright signals from the bladder also confirmed the fast renal clearance and urinary excretion of Magnevist. These results suggest that, although Magnevist represents a good candidate for contrast enhancement in whole-body imaging, its limited targeted specificity may compromise its application for *in vivo* tumor visualization.[25] Importantly, quantitative image analysis of the regions of interest indicated that tumor-to-muscle (T/M) ratios were 61.6-fold higher for MSNPs when compared to Magnevist (Figure 4d).

To assess any *in vivo* cytotoxicity of MSNPs, hematoxylin and eosin (H&E) staining of several organs was carried out after MSNP injection. The histology results showed no acute (6 h) or chronic (2 weeks) tissue injuries in the heart, liver, spleen, lungs or kidneys after administration of MSNPs (Figure S18). Longitudinal tracking of MSNPs in these organs (Figure S19) showed accumulation

of MSNPs at the tumor sites up to 1.5 h post-injection (about 12 % ID/g), which concurs with their enhanced circulation time. This result also confirms the targeting effect of MSNPs, indicative of their high performance in terms of tumor visualization. Body weight monitoring and biochemical tests showed no *in vivo* cytotoxicity of MSNPs (Figures S20 and S21).

In summary, we have developed a smart MRI contrast nanoconjugate based on a combination of $NaGdF_4$ and $CaCO_3$ nanoparticles. The efficient isolation of Gd^{3+} ions from water protons enabled by the rigid framework of the nanoconjugate leads to a silent T_1 signal. The silent mode of T_1 signal can be readily turned on in acidic conditions, where self-assembled nanoconjugate rapidly break apart due to the *in-situ* generation of CO_2 and concomitant release of $NaGdF_4$ nanoparticles. Surface coating of the nanoconjugate with biomimetic cell membranes resulted in a substantial increase in circulation lifetime and tumor-targeting capabilities *in vivo*. The development of $NaGdF_4$–$CaCO_3$ nanoconjugates may revolutionize the study of tumor imaging *in vivo* by providing pH-responsive MRI contrast agents that are more sensitive and selective than those currently in clinical practice.

Experimental Section

The experimental details are provided in the Supporting Information.

Supporting Information

Supporting Information is available from the Wiley Online Library or from the author.

[1]   G. S. Liu, S. R. Banerjee, X. Yang, N. Yadav, A. Lisok, A. Jablonska, J. Xu, Y. Li, M. G. Pomper, P. van Zijl, *Nat. Biomed. Eng.* **2017**, *1*, 977.

[2]   G. J. Lu, A. Farhadi, J. O. Szablowski, A. Lee-Gosselin, S. R. Barnes, A. Lakshmanan, R. W. Bourdeau, M. G. Shapiro, *Nat. Mater.* **2018**, *17*, 456.

[3]   E. Terreno, D. D. Castelli, A. Viale, S. Aime, *Chem. Rev.* **2010**, *110*, 3019.

[4]   Z. Han, X. Wu, S. Roelle, C. Chen, W. P. Schiemann, Z. R. Lu, *Nat. Commun.* **2017**, *8*, 692.

[5]   S. Ogawa, T. M. Lee, A. R. Kay, D. W. Tank, *Proc. Natl. Acad. Sci. USA* **1990**, *87*, 9868.

[6]   M. G. Shapiro, G. G. Westmeyer, P. A. Romero, J. O. Szablowski, B. Küster, A. Shah, C. R. Otey, R. Langer, F. H. Arnold, A. Jasanoff, *Nat. Biotechnol.* **2010**, *28*, 264.

[7]   S. Zhang, M. Merritt, D. E. Woessner, R. E. Lenkinski, A. D. Sherry, *Acc. Chem. Res.* **2003**, *36*, 783.

[8]   M. Bottrill, L. Kwok, N. J. Long, *Chem. Soc. Rev.* **2006**, *35*, 557.

[9]   H. B. Na, I. C. Song, T. Hyeon, *Adv. Mater.* **2009**, *21*, 2133.

[10]   Y. Hou, R. R. Qiao, F. Fang, X. X. Wang, C. Y. Dong, K. Liu, C. Y. Liu, Z. F. Liu, H. Lei, F. Wang, M. Y. Gao, *ACS Nano* **2013**, *7*, 330.

[11]   Z. J. Zhou, R. Tian, Z. Y. Wang, Z. Yang, Y. J. Liu, G. Liu, R. F. Wang, J. H. Gao, J. B. Song, L. M. Nie, X. Y. Chen, *Nat. Commun.* **2017**, *8*, 15468.

[12]   J. S. Ananta, B. Godin, R. Sethi, L. Moriggi, X. W. Liu, R. E. Serda, R. Krishnamurthy, R. Muthupillai, R. D. Bolskar, L. Helm, M. Ferrari, L. J. Wilson, P. Decuzzi, *Nat. Nanotechnol.* **2010**, *5*, 815.

[13]   J. S. Kim, W. J. Rieter, K. M. L. Taylor, H. Y. An, W. L. Lin, W. B. Lin, *J. Am. Chem. Soc.* **2007**, *129*, 8962.

[14]   B. H. Kim, N. Lee, H. Kim, K. An, Y. I. Park, Y. Choi, K. Shin, Y. Lee, S. G. Kwon, H. B. Na, J.-G. Park, T.-Y. Ahn, Y.-W. Kim, W. K. Moon, S. H. Choi, T. Hyeon, *J. Am. Chem. Soc.* **2011**, *133*, 12624.

[15] Y. Lu, Y.-J. Xu, G.-B. Zhang, D. Ling, M.-Q. Wang, Y. Zhou, Y.-D. Wu, T. Wu, M. J. Hackett, B. H. Kim, H. Chang, J. Kim, X.-T. Hu, L. Dong, N. Lee, F. Li, J.-C. He, L. Zhang, H.-Q. Wen, B. Yang, S. H. Choi, T. Hyeon, D. H. Zou, *Nat. Biomed. Eng.* **2017**, *1*, 637.

[16] Z. J. Zhou, C. Q. Wu, H. Y. Liu, X. L. Zhu, Z. H. Zhao, L. R. Wang, Y. Xu, H. Ai, J. H. Gao, *ACS Nano* **2015**, *9*, 3012.

[17] Z. H. Zhao, X. M. Wang, Z. J. Zhang, H. Zhang, H. Y. Liu, X. L. Zhu, H. Li, X. Q. Chi, Z. Y. Yin, J. H. Gao, *ACS Nano* **2015**, *9*, 2749.

[18] T. Kim, E. Momin, J. Choi, K. Yuan, H. Zaidi, J. Kim, M. Park, N. Lee, M. T. McMahon, A. Quinones-Hinojosa, J. W. M. Bulte, T. Hyeon, A. A. Gilad, *J. Am. Chem. Soc.* **2011**, *133*, 2955.

[19] Z. Kovacs, K. N. Green, S. J. Ratnakar, A. D. Sherry, *Chem. Rev.* **2010**, *110*, 2960.

[20] D. L. Ni, W. B. Bu, W. B. Cai, J. L. Shi, *Chem. Soc. Rev.* **2017**, *46*, 7438.

[21] K. N. Raymond, V. C. Pierre, *Bioconjug Chem.* **2004**, *16*, 3.

[22] Y. W. Jun, J. H. Lee, J. Cheon, *Angew. Chem. Int. Ed.* **2008**, *47*, 5122.

[23] H. Y. Xing, S. J. Zhang, W. B. Bu, X. P. Zheng, L. J. Wang, Q. F. Xiao, D. L. Ni, J. M. Zhang, L. P. Zhou, W. J. Peng, K. L. Zhao, Y. Q. Hua, J. L. Shi, *Adv. Mater.* **2014**, *26*, 3867.

[24] Z. L. Dong, L. Z. Feng, W. W. Zhu, X. Q. Sun, M. Gao, H. Zhao, Y. Chao, Z. Liu, *Biomaterials* **2016**, *110*, 60.

[25] P. Mi, D. Kokuryo, H. Cabral, H. Wu, Y. Terada, T. Saga, I. Aoki, N. Nishiyama, K. Kataoka, *Nat. Nanotechnol.* **2016**, *11*, 724.

[26] F. Y. Li, J. X. Lu, X. Q. Kong, T. Hyeon, D. S. Ling, *Adv. Mater.* **2017**, *29*, 1605897.

[27] O. Chen, L. Riedemann, F. Etoc, H. Herrmann, M. Coppey, M. Barch, C. T. Farrar, J. Zhao, O. T. Bruns, H. Wei, P. Guo, J. Cui, R. Jensen, Y. Chen, D. K. Harris, J. M. Cordero, Z. Wang, A. Jasanoff, D. Fukumura, R. Reimer, M. Dahan, R. K. Jain, M. G. Bawendi, *Nat. Commun.* **2014**, *5*, 5093.

[28]   J. Kim, J. E. Lee, S. H. Lee, J. H. Yu, J. H. Lee, T. G. Park, T. Hyeon, *Adv. Mater.* **2008**, *20*, 478.

[29]   F. Wang, R. R. Deng, X. G. Liu, *Nat. Protoc.* **2014**, *9*, 1634.

[30]   A. Parodi, N. Quattrocchi, A. L. van de Ven, C. Chiappini, M. Evangelopoulos, J. O. Martinez, B. S. Brown, S. Z. Khaled, I. K. Yazdi, M. V. Enzo, L. Isenhart, M. Ferrari, E. Tasciotti, *Nat. Nanotechnol.* **2013**, *8*, 61.

[31]   Z. Chen, P. F. Zhao, Z. Y. Luo, M. B. Zheng, H. Tian, P. Gong, G. H. Gao, H. Pan, L. L. Liu, A. Q. Ma, H. D. Cui, Y. F. Ma, L. T. Cai, *ACS Nano* **2016**, *10*, 10049.

[32]   L. Rao, L. L. Bu, B. Cai, J. H. Xu, A. Li, W. F. Zhang, Z. J. Sun, S. S. Guo, W. Liu, T. H. Wang, X. Z. Zhao, *Adv. Mater.* **2016**, *28*, 3460.

[33]   R. Yang, J. Xu, L. G. Xu, X. Q. Sun, Q. Chen, Y. H. Zhao, R. Peng, Z. Liu, *ACS Nano* **2018**, *12*, 5121.

[34]   R. H. Fang, C.-M. J. Hu, B. T. Luk, W. W. Gao, J. A. Copp, Y. Tai, D. E. O'Connor, L. Zhang, *Nano Lett.* **2014**, *14*, 2181.
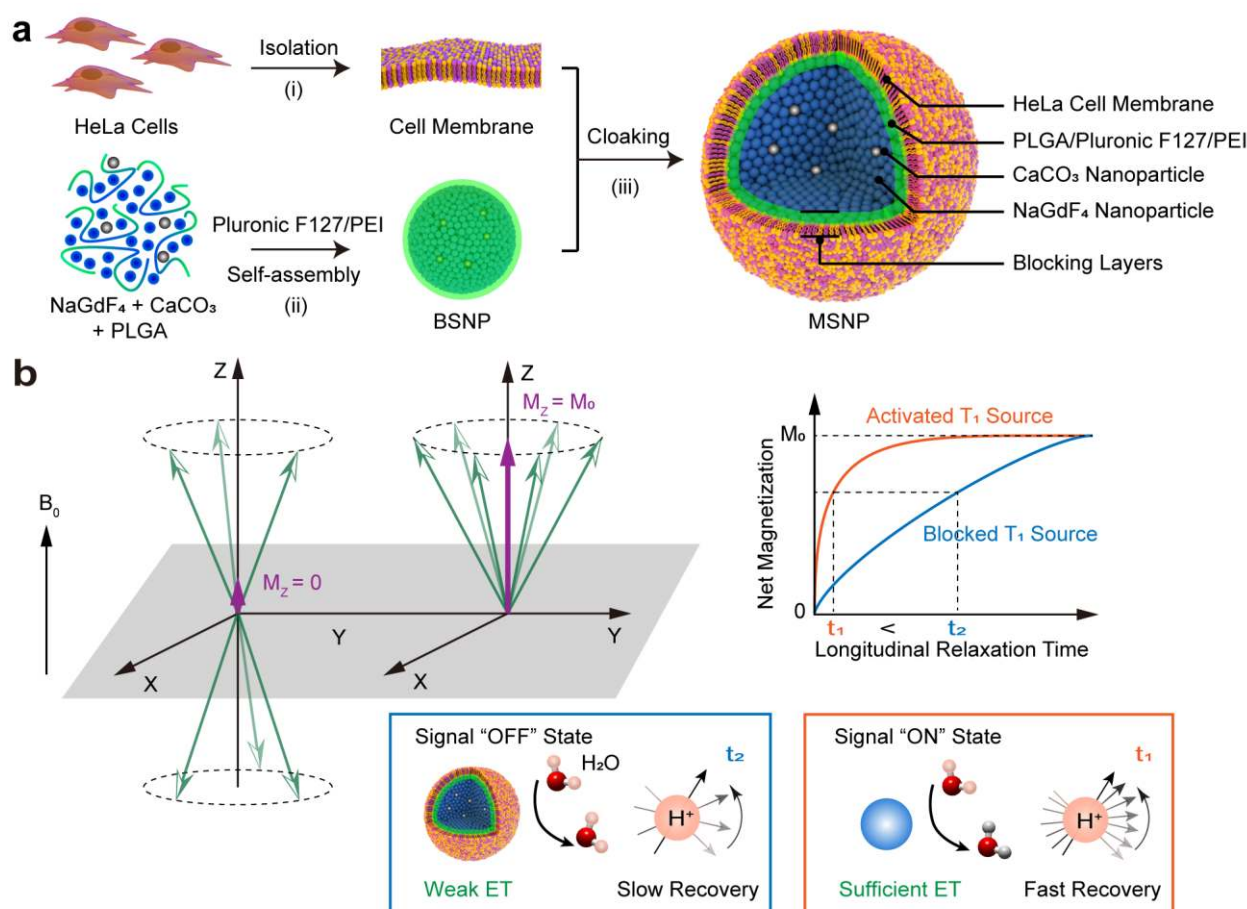
Figure 1. Schematic diagram showing the rationally-designed MSNPs as smart contrast agents for T_1-weighted MRI. (a) The synthetic diagram of MSNPs. (i) Membrane extraction from live HeLa cells. (ii) Assembling BSNPs using nanoparticles ($NaGdF_4$ and $CaCO_3$) as building blocks and polymers (PLGA, Pluronic F127 and branched PEI) as linkers. (iii) Cloaking cell membranes onto the surface of BSNPs. (b) Schematic illustration of the variation in relaxation time of protons upon blocking and activating T_1 source (ultrasmall $NaGdF_4$ nanoparticles). With an external steady-state magnetic field B_0, the spin of protons reaches a steady-state under radiofrequency ($M_Z = 0$, upper left panel). The spin state of protons recovers to the initial state ($M_Z = M_0$) after the radiofrequency disappears. The recovery is facilitated when the T_1-source is activated, and the corresponding longitudinal relaxation time is shortened (upper right panel), resulting in a bright image. Basically, in this design, the spin interaction between crystal lattices and surrounding protons is structurally blocked by multilayers outside the T_1 source (blue line). The energy transfer (ET) from protons to crystal lattices via spin-lattice interaction is then activated due to the pH-responsive capability of MSNPs under acidic microenvironments (orange line).
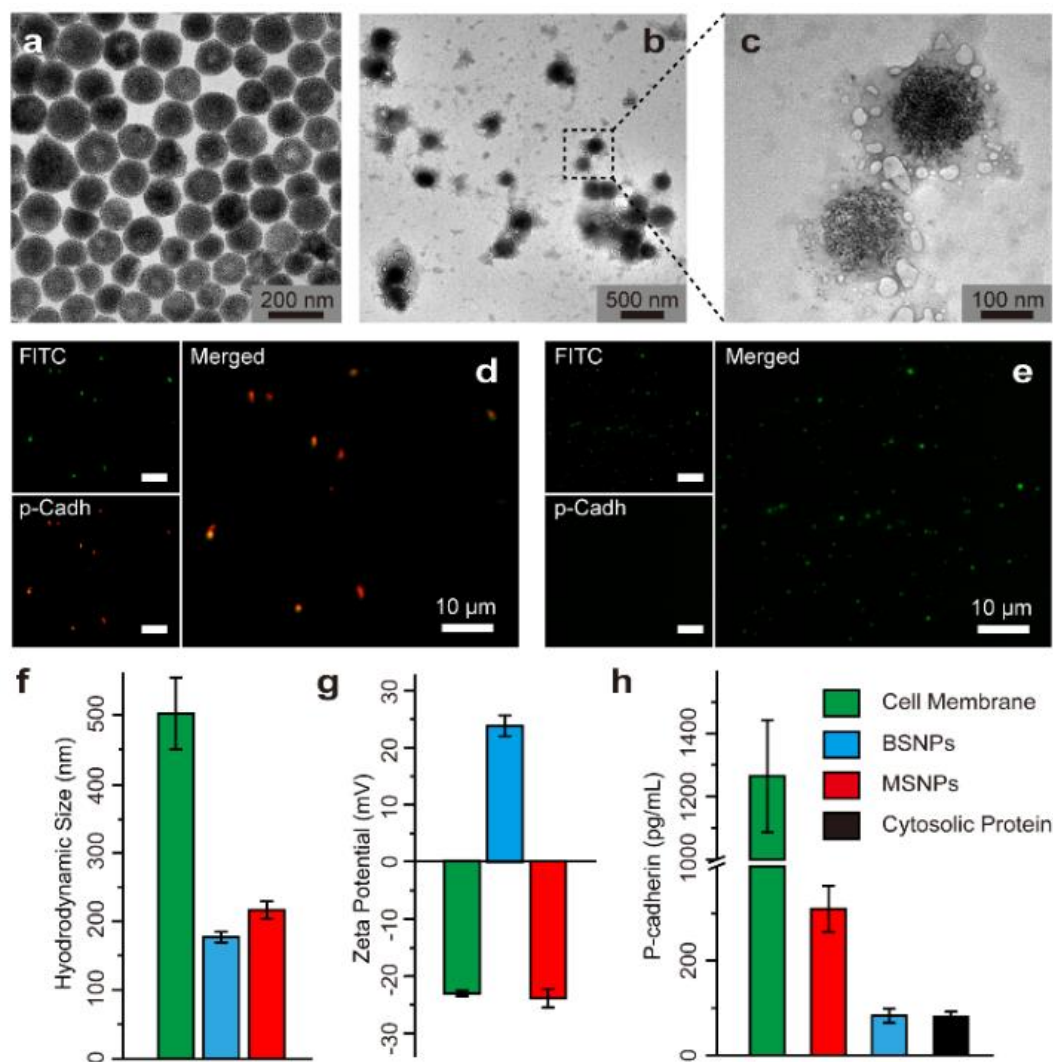
Figure 2. Synthesis and structural characterization of prepared BSNPs and MSNPs. Typical TEM images of BSNPs (a) and MSNPs (b,c). The luminescence microscopy images of MSNPs (d) and BSNPs (e) after treated with FITC salt and anti-*p*-Cadherin antibody in sequence. (f) Hydrodynamic size, (g) zeta potential and (h) ELISA quantitative assays by tracking the amounts of *p*-Cadherin on the surface of HeLa cells, BSNPs and MSNPs. Note that cytosolic protein in h is used as negative control. Values in (f-h) represented as means ± s.d. (n = 3).
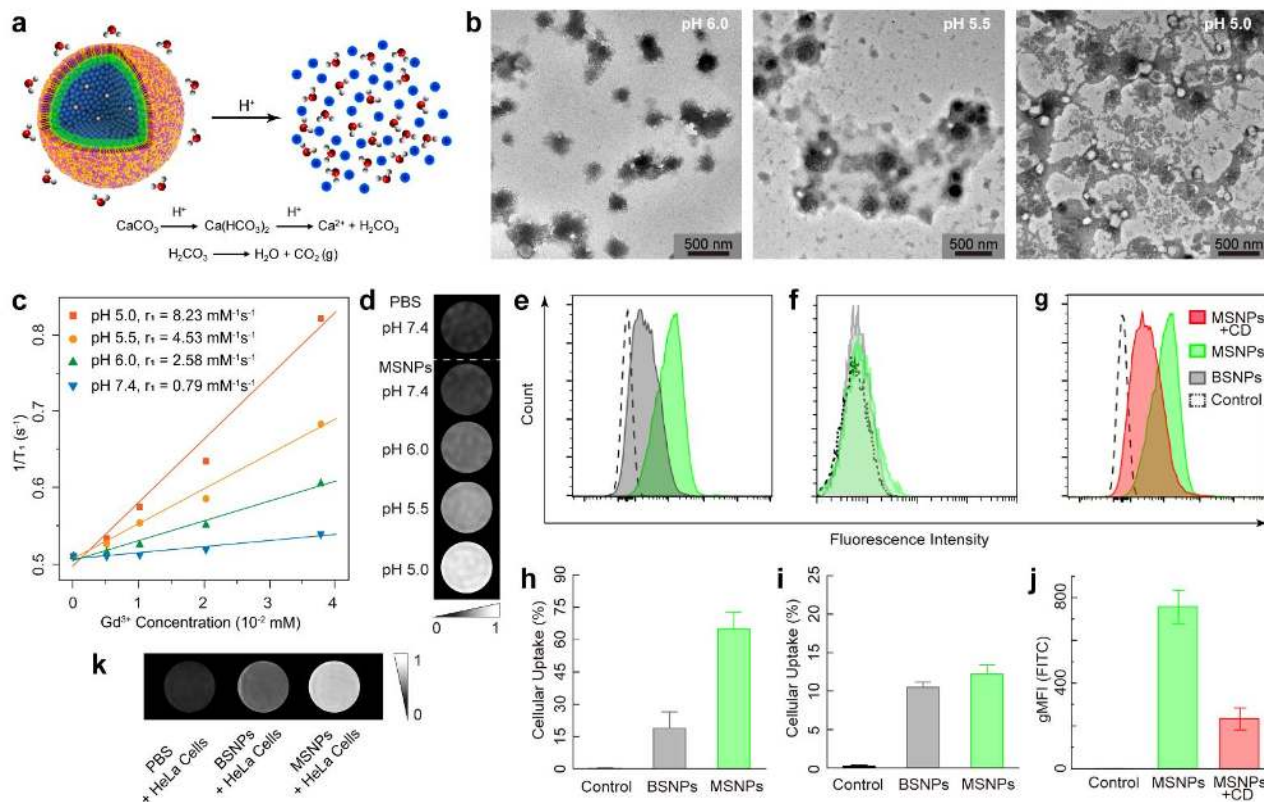
Figure 3. *In vitro* activation of MSNPs. (a) Schematic illustration showing structure disruption of MSNPs in acidic conditions. The reaction formula indicates the generation of carbon dioxide bubbles, which promote the disintegration of nanostructures and the release of $NaGdF_4$ nanoparticles to facilitate spin-lattice interactions between $NaGdF_4$ nanoparticles and water protons. (b) Typical TEM images of MSNPs cultured in PBS buffer solutions with different pH values (6.0, 5.5, 5.0) for 10 min. (c) The plots showing a linear relationship of longitudinal relaxivity of MSNPs versus the concentration of Gd^{3+} ions. (d) The corresponding *in vitro* T_1-weighted MRI phantom images of the solution containing MSNPs in PBS buffer with different pH values. (e,h) Flow cytometry profiles and the corresponding cellular uptake calculation of HeLa cells cultured with BSNPs or MSNPs (0.25 µg/mL FITC). (f,i) Flow cytometry profiles and the corresponding cellular uptake calculation of HepG2 cells cultured with BSNPs or MSNPs (0.25 µg/mL FITC). (g,j) Flow cytometry profiles and histograms showing FITC intensity of HeLa cells cultured with MSNPs without or with the addition of cytochalasin D (CD, 10 µL, 5 µg/mL). (k) *In vitro* T_1-weighted MRI phantom images of HeLa cells microgel solutions pre-treated with pure PBS, BSNPs and MSNPs, respectively. Values represented as means ± s.d. (n=3).
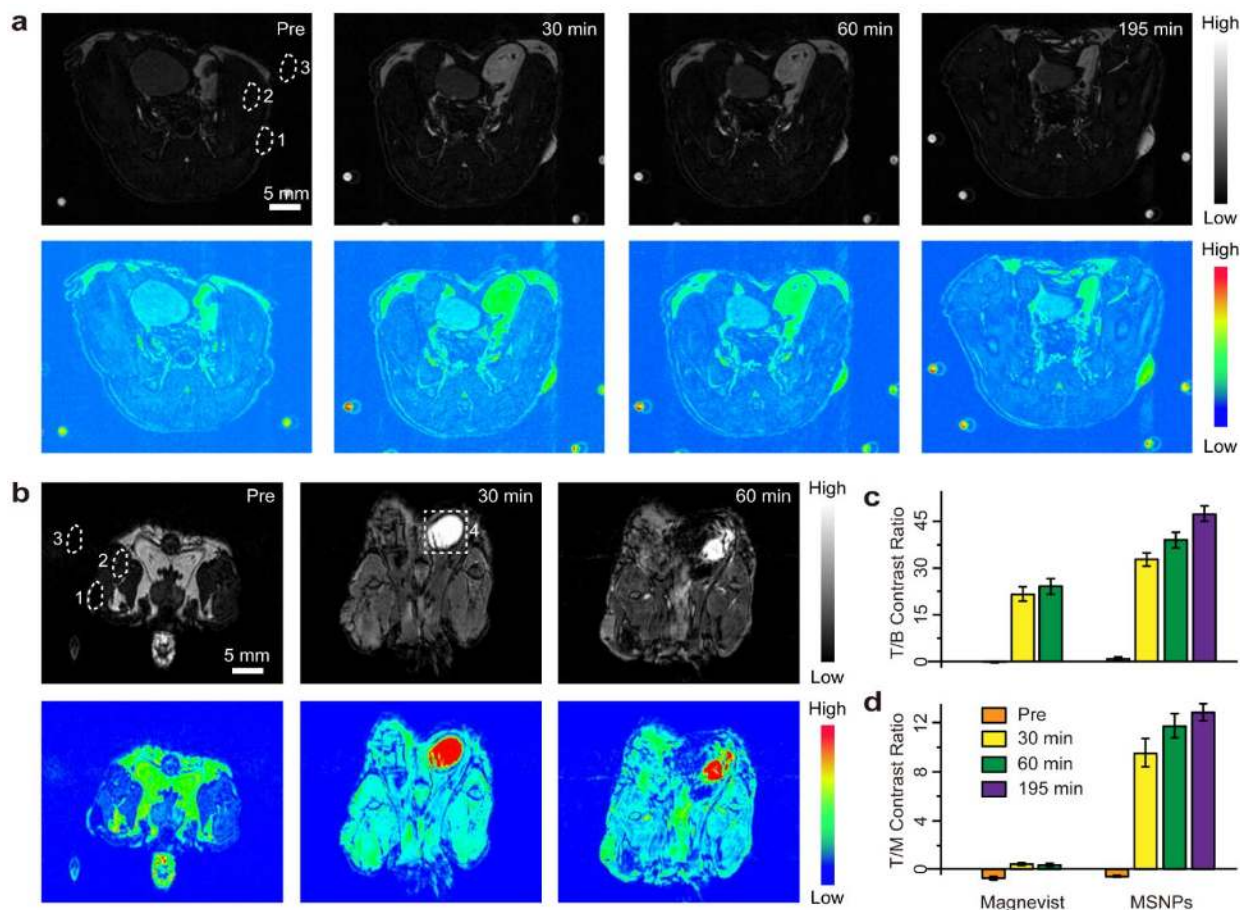
Figure 4. Positive contrast enhancement evaluation in vivo. T_1-weighted MRI and corresponding pseudocolor images of tumor-bearing mice after intravenous injection of (a) MSNPs and (b) Magnevist with the same dosage (2.5 µmol of Gd^{3+} for each mouse). Images were captured before and at different time points after the administration of contrast agents. Dotted circles represent the regions of interest: (1) tumor, (2) muscle, (3) background, (4) bladder. Scale bars are 5 mm for all images. The small spots on the corners are from the circulation apparatus in the MRI scanner. (c,d) Tumor-to-background (T/B) and tumor-to-muscle (T/M) contrast ratios based on the corresponding MRI images. Values represented as means ± s.d. (n = 3).

The table of contents entry:

Commercially available contrast agents, such as Magnevist, for T_1-weighted MRI suffer from short *in vivo* circulating time and a lack of specific targeting to tumor, which hampers their applications in high-performance bioimaging and cancer diagnosis. To this regard, a smart contrast agent comprising cancer cell membranes cloaked $NaGdF_4$–$CaCO_3$ nanoconjugates is designed for amplifying the MRI signal on demand through its sensitive response to mildly acidic tumor microenvironment.

Keywords: gadolinium contrast agents, self-assembly, pH-response, cell membrane cloaking, homogenous targeting

Zhigao Yi, Zichao Luo, Nicole D Barth, Xianfu Meng, Hong Liu, Wenbo Bu, Angelo All, Marc Vendrell, and Xiaogang Liu*

In Vivo Tumor Visualization through MRI Off-On Switching of $NaGdF_4$–$CaCO_3$ Nanoconjugates

TOC Figure: